CHANDRA AND ROSAT OBSERVATIONS OF ABELL 194: DETECTION OF AN X-RAY CAVITY AND MAPPING THE DYNAMICS OF THE CLUSTER

Ákos Bogdán[1], Ralph P. Kraft[1], William R. Forman[1], Christine Jones[1], Ming Sun[2], Christopher P. O'Dea[3], Eugene Churazov[4], and Stefi A. Baum[3]

[1]Smithsonian Astrophysical Observatory, 60 Garden Street, Cambridge, MA 02138, USA
[2]Department of Astronomy, University of Virginia, P.O. Box 400325, Charlottesville, VA 22901
[3]Rochester Institute of Technology, 84 Lomb Memorial Drive, Rochester, NY 14623, USA and
[4]Max-Planck-Institut für Astrophysik, Karl-Schwarzschild-str. 1, 85741 Garching bei München, Germany
Draft version June 20, 2011

ABSTRACT

Based on *Chandra* and *ROSAT* observations we investigated the nearby poor cluster Abell 194, which hosts two luminous radio galaxies, NGC547 (3C 40) and NGC541 (PKS 0123-016A). We demonstrated the presence of a large X-ray cavity ($r \sim 34$ kpc) formed by the giant southern radio lobe arising from 3C 40. The estimated age of the cavity is $t = 7.9 \times 10^7$ years and the total work of the AGN is 3.3×10^{59} erg, hence the cavity power is $P_{cav} = 1.3 \times 10^{44}$ erg s^{-1}. Furthermore, in the *Chandra* images of NGC545 and NGC541 we detected sharp surface brightness edges, identified as merger cold fronts, and extended tails. Using the pressure ratios between inside and outside the cold fronts we estimated that the velocities of NGC545 and NGC541 correspond to Mach-numbers of $M = 1.0^{+0.3}_{-0.5}$ and $M = 0.9^{+0.2}_{-0.5}$, respectively. The low radial velocities of these galaxies relative to the mean radial velocity of Abell 194 imply that their motion is oriented approximately in the plane of the sky. Based on these and earlier observations, we concluded that NGC545 and NGC541 are falling through the cluster, whose center is NGC547, suggesting that Abell 194 is undergoing a significant cluster merger event. Additionally, we detected 20 bright X-ray sources around NGC547 and NGC541, a surprisingly large number, since the predicted number of resolved LMXBs and CXB sources is 2.2 and 4.1, respectively. To explain the nature of additional sources, different possibilities were considered, none of which are satisfactory.

Subject headings: galaxies: active – galaxies: clusters: individual (A194) – galaxies: stellar content – intergalactic medium – X-ray: galaxies: clusters

1. INTRODUCTION

The essential element of the cooling flow problem is that in the centers of galaxy clusters the intracluster medium (ICM) should cool on a timescale much shorter than the Hubble time (Fabian 1994). However, observational evidence from *Chandra* and *XMM-Newton* revealed that only relatively small amounts of gas cools to low temperatures (David et al. 2001; Peterson et al. 2003; Kaastra et al. 2004). The most commonly accepted resolution of this problem is the (re)heating of the ICM by the central active galactic nucleus (AGN) (e.g. Churazov et al. 2001; Peterson & Fabian 2006). In galaxy clusters the most direct signature of the interaction of AGN outbursts and the ICM is the detection of X-ray cavities (e.g. Boehringer et al. 1993; Forman et al. 2005). Outbursts from powerful radio sources can significantly increase the entropy of the ICM thereby inflating the gas distribution and reducing the gas density. Hence at the position of radio lobes a decrement in the X-ray surface brightness becomes observable.

Abell 194 is a poor cluster at a redshift of $z = 0.018$, and hosts two luminous radio sources, 3C 40, associated with NGC547, and PKS 0123-016A, associated with NGC541. The jet emanating from the latter is believed to be responsible for triggering star-formation in Minkowski's Object (van Breugel et al. 1985; Brodie et al. 1985). The extended H-alpha emis-

sion from 3C 40 (e.g. Baum et al. 1988) is associated with a dust disk and diffuse UV emission (Allen et al. 2002), the latter likely to be due to star formation. The nucleus is not detected at 11.8 microns (van der Wolk et al. 2010) and the optical emission line spectrum is low excitation (Buttiglione et al. 2009, 2010), which indicate that the AGN accretion disk is faint – consistent with a low accretion rate.

Abell 194 is one of the most striking "linear" clusters of galaxies, as its galaxy distribution and X-ray emission are both linearly elongated along the northeast-southwest direction (Chapman et al. 1988; Nikogossyan et al. 1999; Jones & Forman 1999). The optical bridge between NGC545/NGC547 and NGC541 (Croft et al. 2006) indicates past and/or recent interactions, thereby suggesting that Abell 194 is not a relaxed cluster. As a consequence of the linear distribution of Abell 194, it has not been clear, whether any of the massive radio galaxies are in the center of the cluster, and whether Abell 194 is undergoing a major merger event. Recently, Sakelliou et al. (2008) investigated the cluster relying on *XMM-Newton* and radio observations. The *XMM-Newton* data did not reveal significant stripping of the intersellar medium of the massive galaxies, and the bending of the radio jets suggested that both NGC547 and NGC541 are moving with subsonic velocities on the order of few hundred km s^{-1}. Thus, Sakelliou et al. (2008) concluded that the central region of Abell 194 is relatively quiescent and is not suffering a major merger event.

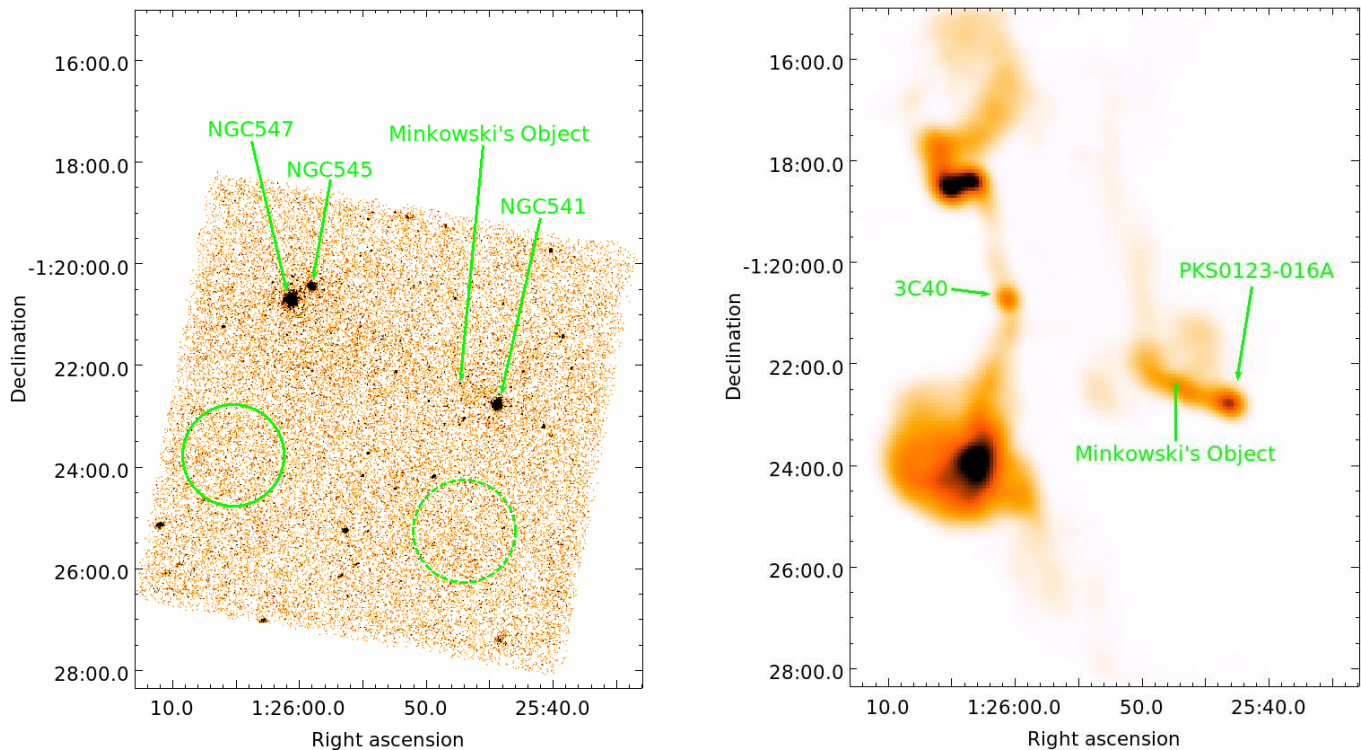E-mail: abogdan@head.cfa.harvard.edu

Fig. 1.— *Left:* 0.98″ Gaussian smoothed *Chandra* (0.3 − 2 keV) ACIS-S3 image of the central 216 × 288 kpc region of Abell 194. The overplotted two circular regions with 21.6 kpc (1′) radius were used to study the surface brightness at the position of the cavity (solid circle) and in a neighboring region (dashed circle). *Right:* 1.4 GHz VLA image of the same region. The bright radio source, 3C 40, is centered on NGC547, whereas PKS 0123-016A is associated with NGC541. Minkowski's object, a region of jet induced star formation, is visible approximately 1′ to the northeast of NGC541.

Hereby we present the results of two *Chandra* pointed observations supplemented with an archival *ROSAT* pointing and complemented with 1.4 GHz Very Large Array (VLA) data to study the connection between the radio jet originating from 3C 40 and the X-ray surface brightness of the ICM. Furthermore, we aim to study the surface brightness distribution of the hot interstellar medium (ISM) of the massive early-type galaxies in Abell 194 relying on the superb angular resolution of *Chandra*, thereby unveiling the dynamics of the cluster. Additionally, we also investigate the origin of the population of bright resolved X-ray sources around the massive early-type galaxies located in Abell 194. Throughout the paper we assume $H_0 = 71$ km s^{-1} Mpc^{-1}, $\Omega_M = 0.3$, and $\Omega_\Lambda = 0.7$ (1″ = 0.36 kpc at $z = 0.018$). The Galactic column density towards Abell 194 is $N_H = 3.78 \times 10^{20}$ cm^{-2} (Dickey & Lockman 1990).

The paper is structured as follows: in Sect. 2 we introduce the analyzed data and describe its reduction. In Sect. 3 we demonstrate the existence of a cavity, and compute the cavity power. The cold fronts in NGC545 and NGC541 and the dynamics of Abell 194 is studied in Sect. 4. The population of bright resolved sources around NGC541, NGC545, and NGC547 is investigated in Sect. 5. The X-ray emission from Minkowski's Object is studied in Sect. 6. Finally, we conclude in Sect. 7.

2. DATA REDUCTION

2.1. *Chandra*

The central part of Abell 194 was observed by two *Chandra* observations on 2007 September 3 for 9.2 ks

(Obs ID: 9583) and on 2007 September 7 for 65.7 ks (Obs ID: 7823) using the ACIS-S detector. The data was processed with CIAO 4.3 and CALDB 4.4.2.

The main steps in the data analyis agree with those outlined in Bogdán & Gilfanov (2008). After filtering flare contaminated time intervals, the total remaining exposure time was 72.3 ks. The data were combined by projecting the shorter observation into the coordinate system of Obs ID 7823. Point sources were detected with the CIAO wavdetect tool in three separate energy bands: in the soft (0.5-2 keV), full (0.5-8 keV), and hard (2-8 keV) bands. The scales on which we searched for sources were the $\sqrt{2}$-series from 1.0 to 8.0, all other parameters of the wavdetect tool were left at default values. The resulting source lists were combined, which was used to study the population of bright X-ray sources and to mask out the point sources for further study of the diffuse emission.

To correct for vignetting and to estimate source detection sensitivities, exposure maps were produced using a power law model with slope of $\Gamma = 1.56$, typical for low-mass X-ray binaries (LMXBs) (Irwin et al. 2003). Assuming this spectrum and 10 photons as a detection threshold, the source detection sensitivity of the combined observation is $\approx 7 \times 10^{38}$ erg s^{-1}. Since the cluster fills the entire field-of-view (FOV) of the ACIS-S3 detector, we used "blank-sky" (http://cxc.harvard.edu/contrib/maxim/acisbg/) observations to subtract the background components. To account for variations in the normalizations of the background, we normalized the background level using the hard band (10-12 keV) count rate ratios.
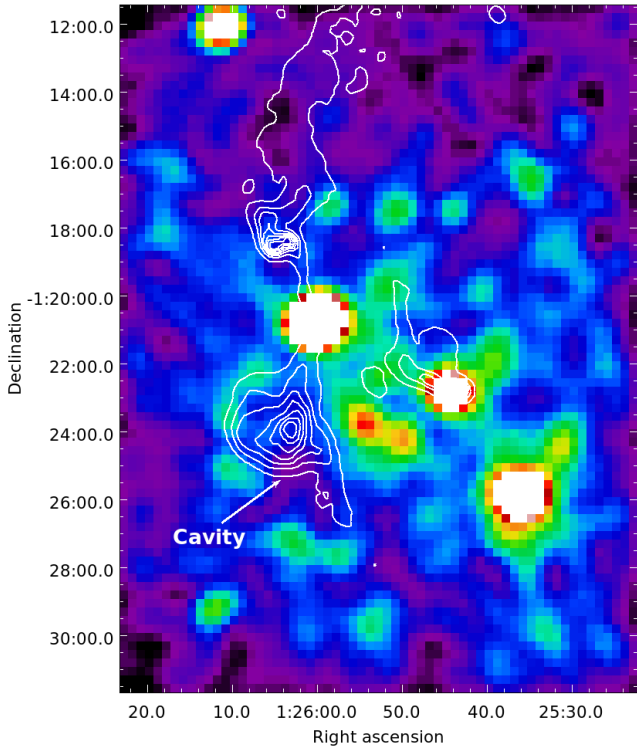
FIG. 2.— $0.5 - 1.5$ keV band background subtracted and vignetting corrected *ROSAT* image of the central 324×432 kpc region of Abell 194 cluster. Overlaid are the intensity levels of the 1.4 GHz VLA image. It is striking that the southern radio lobe is coincident with a clear cavity in the X-ray surface brightness distribution.

2.2. *ROSAT*

ROSAT observed Abell 194 in a pointed PSPC observation on 1992 July 13 for 23.6 ks. Data analysis was performed with standard Xselect tools, vignetting correction was applied using the provided exposure map. Due to the large FOV, the background was subtracted from the outer regions of the detector which is not affected by emission from Abell 194. To study the diffuse emission from the cluster, the brightest point sources were excluded based on the *Chandra* source list, with source cell sizes appropriate for the point spread function of the *ROSAT* PSPC.

2.3. *VLA data*

To study the properties of Abell 194 in radio wavelengths we rely on the 1.4 GHz radio observation taken by the VLA on 1997 September 16 (Fig. 1 right panel). The observation was performed in the VLA C configuration, the mean rms noise in the image is 0.151 mJy/beam. The radio power was computed as $P_\nu = 4\pi D_\nu^2 S_\nu$, where $D_\nu = D_L(1+z)^{-(1+\alpha)/2}$. The bolometric radio luminosity was obtained by integrating the radio flux as

$$L_{\rm radio} = 4\pi D_L^2 S_{\nu_0} \int_{\nu_1}^{\nu_2} (\nu/\nu_0)^{-\alpha} d\nu,$$

where $\nu_1 = 10$ MHz and $\nu_2 = 10000$ MHz and S_{ν_0} is the VLA flux at 1.4 GHz. Additionally, a power law spectrum ($S_\nu \propto \nu^{-\alpha}$) is assumed, where α is the spectral index. The exact value of α is somewhat uncertain: Andernach et al. (1980), Kuehr et al. (1981), and
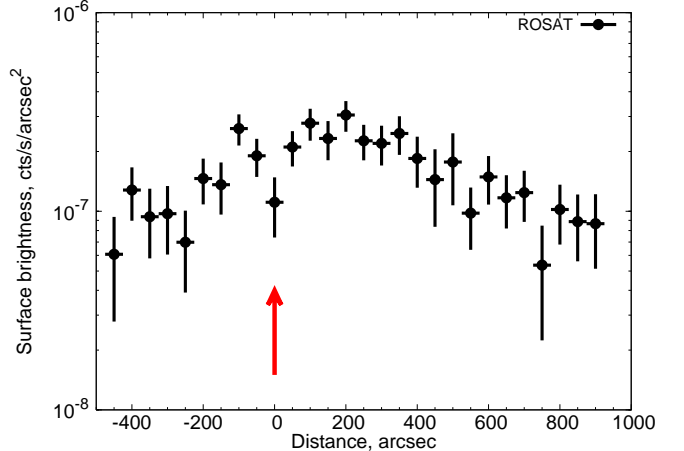

FIG. 3.— Surface brightness distribution of the $0.5-1.5$ keV band *ROSAT* PSPC image. Background components are subtracted and vignetting correction is applied. On the x-axis distance is measured from the peak of the radio emission and shows the decrement in the X-ray surface brightness (arrow). The values along the x-axis decrease towards east.

Spinrad et al. (1985) give spectral indices of 0.7, 0.87, and 0.66, respectively. In the further discussion we adopted the mean of these values, namely $\alpha = 0.74$.

2.4. *Two-Micron All Sky Survey*

To trace the stellar light of the massive early-type galaxies in Abell 194, we used the Two-Micron All Sky Survey (2MASS) Large Galaxy Atlas (LGA) (Jarrett et al. 2003), which is commonly applied for this purpose (e.g. Bogdán & Gilfanov 2010). Since the 2MASS K-band images of Abell 194 are not background subtracted, we used nearby regions off the galaxies to estimate the background level. To convert counts to luminosity, we assumed that the absolute K-band magnitude of the Sun is $M_{K,\odot} = 3.28$.

3. THE X-RAY CAVITY

3.1. *Detection of the cavity*

In the right panel of Fig. 1 we show the 1.4 GHz VLA image of the central 216×288 kpc region of Abell 194. The image is dominated by giant radio lobes originating from 3C 40, which extend up to ~ 100 kpc. Note that the southern lobe is within the FOV of the ACIS-S3 detector. On the western side of the image another, much less prominent, jet is observable from PKS 0123-016A, which triggers star-formation in Minkowski's Object (Sect. 6). In the left panel of Fig. 1 we present a $0.98''$ Gaussian smoothed $0.3 - 2$ keV band *Chandra* ACIS-S3 image of the same region. The image was background subtracted and corrected for vignetting as described in Sect. 2.1. The most striking objects on the image are the three massive early-type galaxies, two of them hosting bright AGN. Additionally, truly diffuse emission is also present, which is concentrated in the region enclosed by NGC547 and NGC541.

The large radio lobes indicate a relatively recent outburst from 3C 40. In general, jets extending outside from the central AGN inflate radio lobes, thereby pushing the X-ray emitting gas away and creating bubbles or relativistic plasma. The directly observable consequence of this process is the detection of cavities in the X-ray surface brightness distribution. Therefore in Abell 194

we expect to observe a decrement in the X-ray surface brightness at the position of the radio lobe. To unveil such a decrement we studied *Chandra* and *ROSAT* data.

First, we studied the $0.3 - 2$ keV band *Chandra* image to identify the cavity. We selected two circular regions with $1'$ diameter on the southern part of the cluster, marked on the left panel of Fig. 1. One region is centered at the expected position of the cavity (RA: 01h26m05.2s; Dec: -01d23m46.1s), whereas the other is located in the south-western part of the cluster (RA: 01h25m47.0s; Dec: -01d25m15.8s). If an X-ray decrement exists, a significantly lower X-ray flux is expected from the former region. The observed counts from both regions were converted into flux using an optically-thin thermal plasma emission model (MEKAL model in XSPEC) with $kT = 3.0$ keV, which is the best-fit temperature of the ICM. The obtained flux in the cavity-region is $F_1 = (2.95 \pm 0.15) \times 10^{-14}$ erg s^{-1} cm^{-2}, and is significantly lower than the neighboring region, $F_2 = (3.75 \pm 0.16) \times 10^{-14}$ erg s^{-1} cm^{-2}. This suggests the existence of an X-ray cavity coincident with the southern 3C 40 radio lobe.

Second, to confirm the existence of the cavity, we investigated the available *ROSAT* PSPC data, whose major advantages are its low background level and its large FOV. In Fig. 2 a $0.5 - 1.5$ keV band vignetting corrected and background subtracted *ROSAT* image is shown, overlaid are the 1.4 GHz VLA contours. The image shows that the hot ICM fills the cluster, and reveals an X-ray decrement, coincident with the southern radio lobe. To further illustrate the presence of the cavity we show the $0.5 - 1.5$ keV band X-ray surface brightness distribution in Fig. 3. The profile was obtained using rectangular boxes oriented in the east-west direction, whose extent were $50'' \times 125''$. The region at $0''$ distance is centered in the peak of the radio emission, i.e. in the center of the X-ray cavity. Note that the profile is corrected for vignetting and background is subtracted as described in Sect. 2.2. In agreement with our previous observations, Fig. 3 reveals a sharp drop at the expected position of the X-ray cavity, and shows a relatively smooth gas distribution elsewhere.

Thus, *Chandra* and *ROSAT* results demonstrate the existence of an X-ray cavity in Abell 194, produced by the giant southern radio lobe arising from 3C 40.

3.2. *Cavity power*

Measuring the cavity power ($P_{\rm cav}$) offers a straightforward estimate of the energy injected to the X-ray emitting gas by the AGN outburst. $P_{\rm cav}$ can be estimated by computing the minimal energy required to inflate the cavity and the age of the cavity. The former is obtained by measuring the cavity enthalpy as $H = 4pV$ (for relativistic plasma), whereas the latter is calculated as the sound crossing time.

The detected cavity in Abell 194 is described with a circular region with a radius of 34 kpc ($\approx 1.57'$) centered on the coordinates: RA: 01h26m05.2s, Dec: -01d23m46.1s. The gas distribution within the cavity is assumed to be spherically symmetric. Since the ICM is not strongly peaked in Abell 194, we used the average ICM properties within the *Chandra* FOV to obtain the physical parameters of the gas. Therefore we selected a circular region with $4'$ radius centered in the center

of the ACIS-S3 detector. Note that resolved point sources were excluded along with three circular regions around NGC541, NGC545, and NGC547 with radii of $15''$, $13''$, and $13''$, respectively. The spectra of the $4'$ large region was described with an optically-thin thermal plasma emission model (MEKAL model in XSPEC) with a best-fit temperature of $kT = 3.02^{+0.26}_{-0.31}$ keV. From the normalization of the model the emission measure is $\int n_e n_H dV = 3.0 \times 10^{65}$ cm^{-3}, implying an average density of $n = 1.9 \times 10^{-3}$ cm^{-3}. Thus, the average pressure is $p = 1.9 n_e kT = 1.7 \times 10^{-11}$ erg cm^{-3}. Using these parameters and computing the volume of the cavity region, the total AGN work is deduced as $4pV = 3.3 \times 10^{59}$ erg.

To compute the cavity power from the $4pV$ work, the age of the cavity has to be estimated. To apply a realistic expansion velocity, we consider two observational facts. On the one hand the lack of a shock indicates that the expansion of the lobe is not very supersonic, on the other the lobe is not strongly deformed by the buoyancy force hence the expansion is also not very subsonic. Therefore, a somewhat uncertain but reasonable assumption is that the radio lobes propagate with the sound speed, which, in a $kT = 3.0$ keV plasma, is $c_s = \sqrt{(\gamma kT)/(\mu m_H)} = 875$ km s^{-1} by adopting $\gamma = 5/3$ and $\mu = 0.62$. As the center of the cavity is approximately $d = 71$ kpc ($\approx 3.3'$) from 3C 40, the cavity age is $t = d/c_s = 7.9 \times 10^7$ years. Based on these, the cavity power of the southern cavity is $P_{\rm cav} = 4pV/t = 1.3 \times 10^{44}$ erg s^{-1}.

3.3. *Comparison with other ratio induced cavities*

During the operation of *Chandra* the existence of radio induced X-ray cavities has been shown in many galaxies and galaxy clusters. The correlation between the cavity power ($P_{\rm cav}$) and the corresponding radio luminosity ($L_{\rm radio}$) was studied in a broad sample of systems by Birzan et al. (2004, 2008). The best-fit relation for the total source luminosity, given by Birzan et al. (2008) is:

$$\log P_{\rm cav} = (0.48 \pm 0.07) \log L_{\rm radio} + (2.32 \pm 0.09),$$

where $L_{\rm radio}$ represents the bolometric radio luminosity. In this relation both $P_{\rm cav}$ and $L_{\rm radio}$ are in units of 10^{42} erg s^{-1}. Since the detected cavity in Abell 194 is similar to those investigated earlier (Birzan et al. 2004, 2008), we examine if its properties fit this relation.

The bolometric radio luminosity was computed from the 1.4 GHz VLA data as described in Sect. 2.3, which yielded $L_{\rm radio} = 1.7 \times 10^{41}$ erg s^{-1}, whereas the cavity power is $P_{cav} = 1.3 \times 10^{44}$ erg s^{-1} (Sect. 3.2). Substituting the observed radio luminosity in the Birzan et al. (2008) relation, we find that the corresponding predicted cavity power is about 8.9×10^{43} erg s^{-1}. This value is similar albeit somewhat lower than the observed cavity power in Abell 194. Considering the uncertainties in the estimation of P_{cav}, and the dispersion in the relation given by Birzan et al. (2008), we conclude that the detected cavity in Abell 194 is in good agreement with those obtained in other galaxies and clusters of galaxies.

4. COLD FRONTS IN NGC545 AND NGC541 AND LARGE SCALE DYNAMICS IN ABELL 194

4.1. *Cold fronts in NGC545 and NGC541*

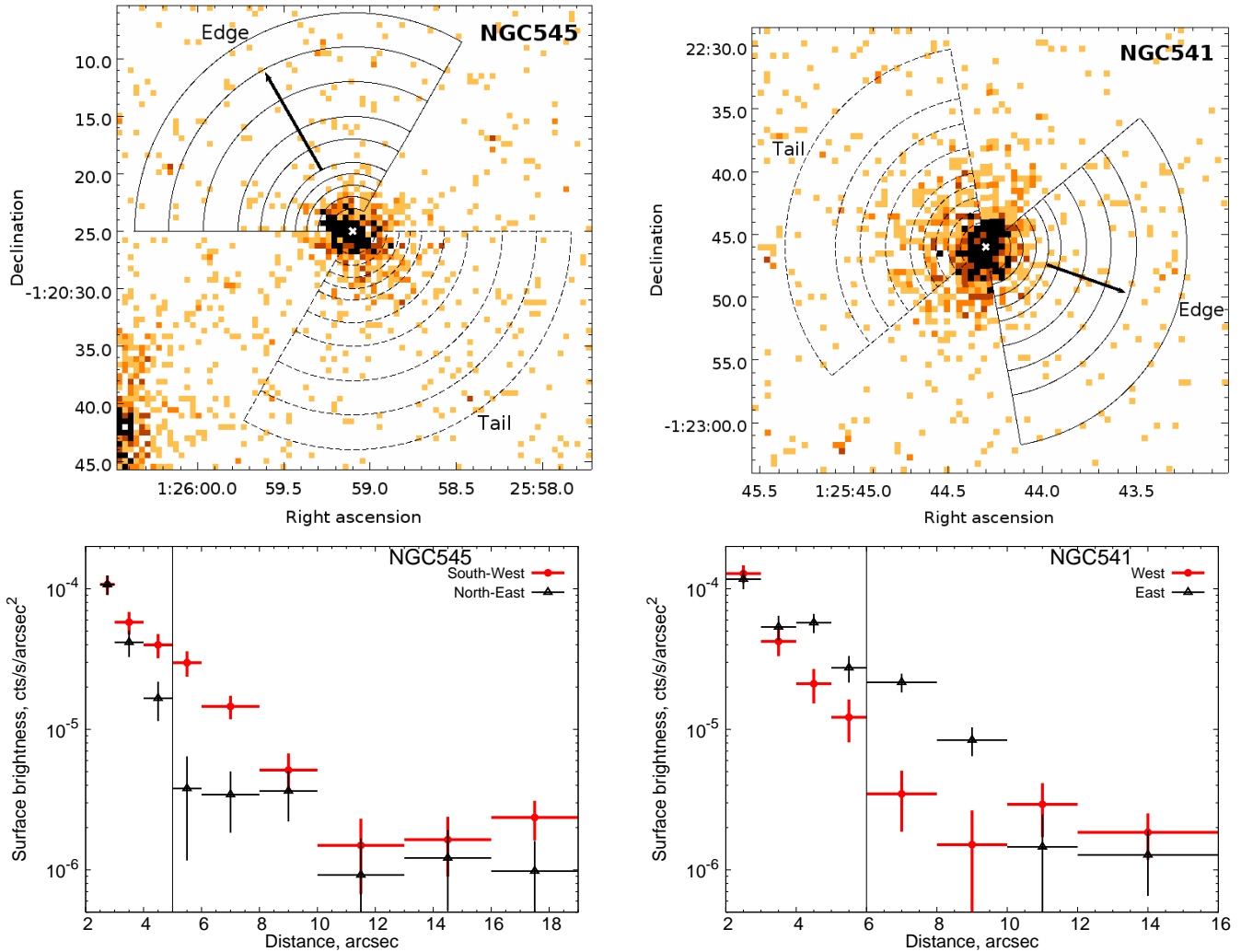Two galaxies in Abell 194, namely NGC545 and NGC541, exhibit sharp surface brightness edges and ex-

FIG. 4.— *Top:* $0.3 - 2$ keV *Chandra* images of NGC545 (left panel) and NGC541 (right panel). Overplotted are the regions used to obtain surface brightness profiles shown in the bottom panels. The arrows show the approximate direction of motion of NGC545 and NGC541 (Sect. 4.2). The center of galaxies is marked with the cross. *Bottom:* X-ray surface brightness distributions in the $0.3 - 2$ keV energy range around NGC545 and NGC541 using the regions shown in the upper panels. Filled circles (red) represent the western and south-western sides, whereas triangles (black) illustrate the eastern and north-eastern sides of NGC545 and NGC541, respectively. The thin vertical lines mark the approximate position of the surface brightness edges.

tended tails in the soft band *Chandra* images (Fig. 4 upper panels). The edges are located on the north-eastern and western side of NGC545 and NGC541, respectively. To demonstrate the existence of the edges and tails, we extracted surface brightness profiles of the galaxies using the regions displayed in the upper panels of Fig. 4. The background subtracted $0.3 - 2$ keV band profiles are depicted in the lower panels of Fig. 4. As suggested by the images the X-ray surface brightness cuts at $\sim 5''$ on the north-eastern and western sides of NGC545 and NGC541, whereas on the opposite sides it extends beyond $\sim 10''$ radius.

To further study the X-ray emission inside and outside the edges, we extracted X-ray energy spectra from both regions. Due to the relatively low number of counts only one region could be investigated inside and outside the edges. The former was represented by circular regions centered each galaxy with $5''$ and $6''$ radius for NGC545 and NGC541, respectively. The soft emission was de-scribed with a MEKAL model and the abundances were fixed at 0.5 solar (Anders & Grevesse 1989). The best-fit temperatures were 0.63 ± 0.07 keV and 0.55 ± 0.06 keV for NGC545 and NGC541, respectively. Regions outside the edges were represented by similar wedges to those depicted in Fig. 4, but their radial extents were $5'' - 75''$ and $6'' - 75''$ for NGC545 and NGC541, respectively. The regions were oriented towards the north-eastern side of NGC545 and the western side of NGC541. The spectra demonstrated the presence of ICM, which emission was described with a MEKAL model with abundances fixed at 0.3 solar. The best-fit temperatures were $3.2^{+1.2}_{-0.7}$ keV in NGC545 and $2.8^{+1.1}_{-0.7}$ keV in NGC541.

The observed sharp surface brightness edges in NGC545 and NGC541, furthermore the temperature difference between the regions inside and outside the edges suggest that these features are contact discontinuities or cold fronts (Vikhlinin et al. 2001; Machacek et al. 2005;

Markevitch & Vikhlinin 2007).

4.2. *Large scale dynamics of Abell 194*

The detection of cold fronts in NGC545 and NGC541 permits to compute their velocity, hence map the large scale dynamics of Abell 194. Ideally, their velocities can be directly calculated from X-ray observations using the ratio of the thermal pressures at the stagnation point (p_0) and in the free stream (p_1) (Vikhlinin et al. 2001). However, due to the relatively low number of counts a number of assumptions are involved hence only crude estimates can be given. On the one hand p_0 cannot be constrained across the surface brightness edges, instead we used the average pressure in the galaxy; on the other p_1 can only be measured in a relatively large region outside the cold fronts. Thus, we assume that no significant temperature and pressure gradients are present inside and outside the galaxies. Additionally, the poorly constrained abundances further limit the accuracy of the estimates.

The pressure ratios were estimated using the regions described in Sect. 4.1. We derived $p_0/p_1 = 2.1^{+0.7}_{-0.9}$ for NGC545 and $p_0/p_1 = 1.8^{+0.5}_{-0.7}$ for NGC541, which translate to Mach numbers of $M = 1.0^{+0.3}_{-0.5}$ for NGC545 and $M = 0.9^{+0.2}_{-0.5}$ for NGC541. The sound speed in 3 keV gas is $c_s = 875$ km s^{-1}, hence the Mach numbers correspond to velocities of 875^{+263}_{-438} km s^{-1} and 788^{+175}_{-438} km s^{-1} for NGC545 and NGC541, respectively.

Based on the velocities of NGC545 and NGC541 and their radial velocities, the orientation of the galaxy motions can be deduced. The radial velocities of NGC545 and NGC541 are 5338 km s^{-1} and 5422 km s^{-1} (NED), implying a velocity of -96 km s^{-1} and 26 km s^{-1} relative to the mean radial velocity of Abell 194 (5396 km s^{-1}). Thus, we conclude that both NGC545 and NGC541 are moving essentially in the plane of the sky, since the direction of their motion differs $\lesssim 10°$ from it.

The observed cold fronts and the estimated transonic velocities of NGC545 and NGC541 suggest that they are falling through the cluster. The gas distribution in NGC547 appears to be symmetric and does not reveal any surface brightness edges or tails, indicating its relatively low velocity. Indeed, from the bending of the radio jet emanating from 3C 40 Sakelliou et al. (2008) estimated that NGC547 moves with subsonic velocity, $v_{\mathrm{NGC547}} \leq 300$ km s^{-1}. Additionally, the radial velocities of NGC547, NGC545, and NGC541 are very similar to each other: 5468 km s^{-1}, 5338 km s^{-1}, and 5422 km s^{-1}, respectively. The minor differences in the radial velocities and the small projected distances between these galaxies suggest that they compose a gravitationally bound system. Thus, the center of Abell 194 is presumably NGC547, and NGC545 and NGC541 are falling through the cluster, implying that Abell 194 is undergoing a significant cluster merger event.

The non-detection of large scale cold fronts in Abell 194 indicate that the merger is not between two roughly equal mass systems in the first pass stage. Instead, the galaxies may have already undergone more than one pass, during which most of the cold gas was stripped from them. In agreement with this, the optical/X-ray bridge between NGC547/NGC545 and NGC541 (Croft et al. 2006) also indicates past and/or recent interactions between them,

implying that the potential probably extends to the western side of the cluster as well.

5. OVERDENSITY OF BRIGHT SOURCES AROUND MASSIVE EARLY-TYPE GALAXIES IN ABELL 194

5.1. *Predicted number of LMXBs and CXB sources*

A surprising result of our analysis is that around the massive early-type galaxies of Abell 194 (NGC541, NGC545, NGC547) an unusually high number of bright resolved sources are observed (Fig. 5). To study the number of sources around these galaxies, two circular regions were selected with $1'$ radius: the first is centered between NGC547 and NGC545 (henceforth region A) whereas the second is centered on NGC541 (henceforth region B). The central parts ($15''$ for NGC547 and $13''$ for NC541 and NGC545) of galaxies were excluded from the analysis since their bright X-ray coronae notably reduce the point source detection sensitivity. Considering only sources with at least 10 net counts in the $0.5 - 8$ keV energy range, in regions A and B 11 and 9 sources were detected, respectively.

The most likely origins of the detected sources are: first, they could be low-mass X-ray binaries (LMXBs) associated with the galaxies; second, they may be resolved cosmic X-ray background (CXB) sources.

The number of resolved LMXBs above a certain sensitivity limit can be determined using their average luminosity function (Gilfanov 2004). In the selected regions the source detection sensitivity is $\approx 7.2 \times 10^{38}$ erg s^{-1}. The corresponding K-band luminosities are 2.4×10^{11} L$_{\mathrm{K},\odot}$ and 1.5×10^{11} L$_{\mathrm{K},\odot}$ in regions A and B, respectively. According to the LMXB luminosity function we predict 0.8 and 0.5 resolved LMXBs above the detection threshold in regions A and B, respectively. Thus, only $\approx 6\%$ of the resolved sources can be explained by LMXBs.

The number of predicted CXB sources were determined using two independent approaches. As a first method, we used the $\log N - \log S$ function of Moretti et al. (2003). We converted the observed $0.5 - 8$ keV band sensitivity limit (1.14×10^{-15} erg s^{-1} cm^{-2}) to the $2 - 10$ keV band assuming a power law spectral model with $\Gamma = 1.4$ and Galactic column density, which results in the sensitivity limit of 1.03×10^{-15} erg s^{-1} cm^{-2}. Based on this value, the surface area of regions A and B, and the $\log N - \log S$ function, we predicted 1.9 and 2.0 sources in A and B regions, respectively. As a second method, we used the field of Abell 194 to determine the average surface density of resolved CXB sources. Using a circular region with $3'$ diameter, centered in the CCD, 17 point sources were observed. Note that in this computation the sources located within regions A and B are excluded, along with the point source associated with the elliptical galaxy CGCG 385-127. Based on the surface area of regions A and B, we expect 2.0 and 2.1 sources within these regions. We stress that the predicted numbers of CXB sources obtained with the two methods are in excellent agreement with each other. Therefore no more than $\approx 20\%$ of the detected sources could arise from resolved CXB sources.

Based on these, in the first instance, we find that LMXBs and CXB sources altogether can be responsible for ≈ 5.4 sources, whereas the observed number is 20, implying a $> 5\sigma$ excess of point sources. We men-
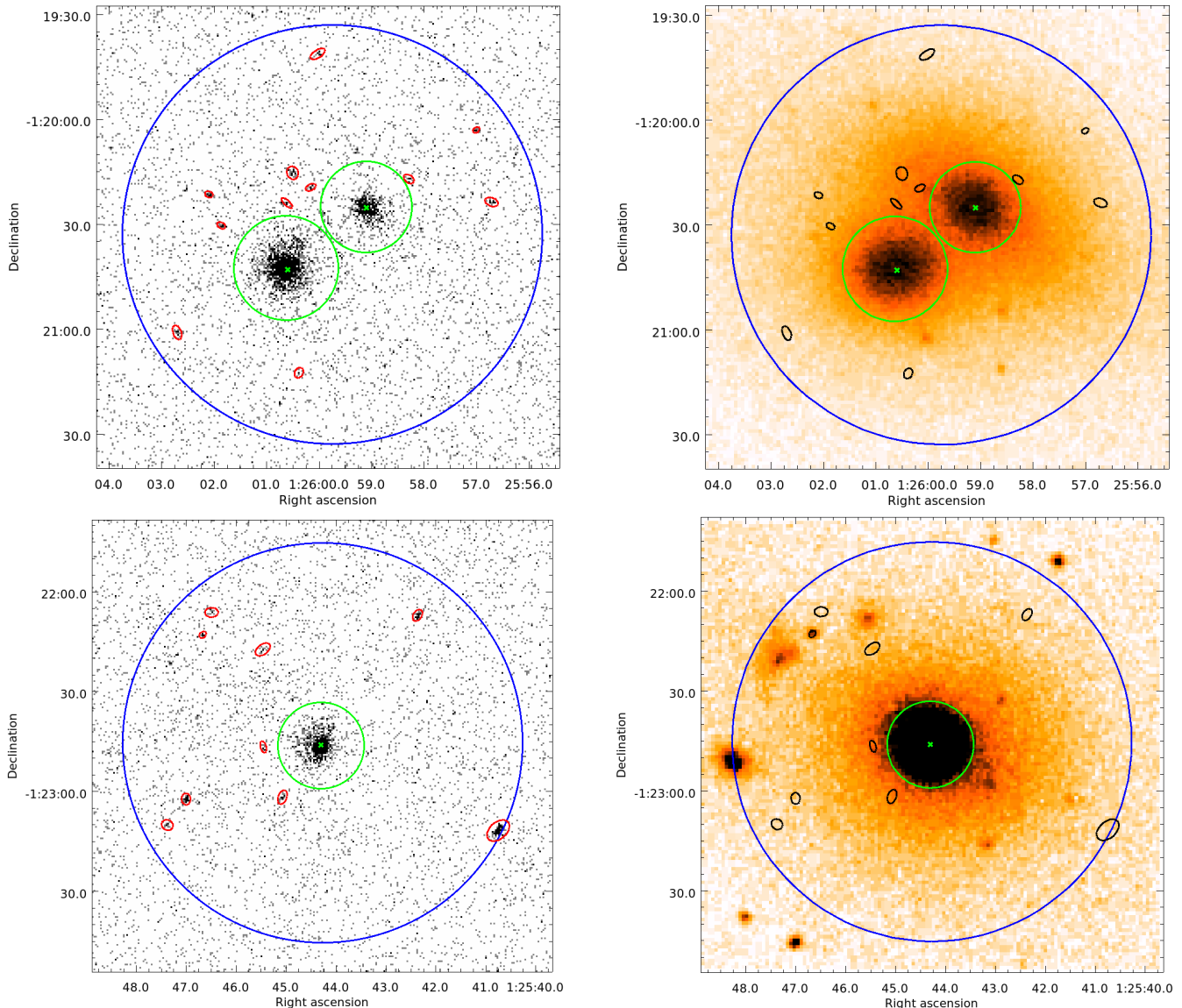
FIG. 5.— *Left:* $0.5 - 8$ keV band *Chandra* image of the NGC547, NGC545 regions (top panel) and NGC541 region (bottom panel). The large circle (blue) represents the $1'$ regions around the galaxies, whereas the small (green) circles ($15''$ for NGC547 and $13''$ for NGC545 and NGC541) show the regions excluded from the analyses. The detected point sources having at least 10 net counts are also encircled. The center of galaxies is marked with the cross. *Right:* DSS R-band images of the same regions as on the left panel. The meaning of the circles is the same as before. Note, that only one X-ray source on the north-eastern part of NGC541 (bottom) has an optical counterpart.

tion that Hudaverdi et al. (2006) reported an excess of sources in Abell 194 (and Abell 1060) in the luminosity range $10^{39.6} \leq L_X \leq 10^{41.4}$ erg s^{-1} over the full *XMM-Newton* FOV. They suggested that these sources, many identified with cluster member galaxies, are AGN within cluster-member galaxies. The source excess we report has a very different origin since these sources appear to be associated with the massive early-type galaxies in Abell 194, and are fainter, typically $L_X \sim 10^{39}$ erg s^{-1}, than those studied by Hudaverdi et al. (2006).

5.2. *Possible origin of the source overdensity*

The normalization of the LMXB luminosity function exhibits a scatter of about a factor of two (e.g. Gilfanov 2004). Although such variations cannot explain the to-

tal number of excess sources, it may be responsible in part. The stable shape of the luminosity function implies that if its bright end normalization is higher, then its faint end must also have an elevated level. Thus, we can scale the average luminosity function using the $2 - 8$ keV band flux from the unresolved emission in regions A and B. The derived total hard band unresolved X-ray luminosity of $L_X = 3.9 \times 10^{40}$ erg s^{-1} corresponds to $L_X/L_K = 1.0 \times 10^{29}$ erg s^{-1} L$_{K,\odot}^{-1}$. Below the 7.2×10^{38} erg s^{-1} sensitivity limit, the average LMXB luminosity function (Gilfanov 2004) predicts $L_X/L_K = 5.9 \times 10^{28}$ erg s^{-1} L$_{K,\odot}^{-1}$ in the $2 - 8$ keV energy band, assuming an average power law LMXB spectrum with slope of $\Gamma = 1.56$ and Galactic column den-

sity (Irwin et al. 2003). Thus, the luminosity function of LMXBs has to be scaled up by $\approx 70\%$. Therefore the total predicted number of LMXBs is 2.2 in regions A and B. Taking this as the expectation value, the total number of predicted LMXBs and CXBs is 6.3, whereas 20 sources are observed.

An additional major uncertainty in the average LMXB luminosity function is the relatively low number of bright $(L_X \gtrsim 8 \times 10^{38}$ erg s$^{-1})$ sources in the sample of Gilfanov (2004). This implies large systematic uncertainties at the bright end of the luminosity function. Indeed, according to Gilfanov (2004) the number of birght LMXBs above $L_X \gtrsim 8 \times 10^{38}$ erg s^{-1} may be factor of ~ 4 times higher within 90% confidence interval due to systematic errors. Taking this uncertainty into account, it is feasible that significantly more, altogether $8-9$, resolved sources are bright LMXBs in regions A and B. Therefore LMXBs and CXB sources may account for up to 11 sources out of the 20 detected.

Since no significant star-formation is associated with early-type galaxies, it is implausible that the additional population of point sources are high-mass X-ray binaries (HMXBs). To illustrate this point we estimate the star-formation rate (SFR) required to produce 9 HMXBs brigher than 7.2×10^{38} erg s^{-1}. Relying on the average HMXB luminosity function from Grimm et al. (2003) and using the normalization by Shtykovskiy & Gilfanov (2005) the required SFR is ~ 18 M$_\odot$/yr. As this value is consistent with those observed for starburst galaxies, we conclude that the importance of HMXBs is negligible.

Since the galaxies we consider are in a cluster, it is possible that (at least some of) the X-ray sources are associated with galaxies within the cluster, alternatively foreground stars may play a role. To identify such galaxies we cross-checked the coordinates of all X-ray sources in NED. Additionally we visually inspected Hubble Space Telescope and DSS images (Fig. 5 right panel) to search for optical counterparts of X-ray sources. We found only one X-ray source around NGC 541 (RA: 01h25m46.66s; Dec: -01d22m12.97s) which has an optical counterpart. Excluding this source the observed number of X-ray sources is 19, whereas LMXBs and CXB sources may account up to 11 sources.

As is clear from Fig. 5, NGC547, NGC545, and NGC541 have very luminous X-ray coronae extending to large radii, within which a notable fraction of the detected sources are located. As our experience shows, it is feasible that some (unknown) fraction of the resolved sources are not pointlike compact sources, but are features of the shock-heated gas distribution. Obviously, such features in the gas distribution would further decrease the discrepancy between the observed and predicted number of resolved pointlike sources. However, taking the depth of the *Chandra* observations and the distance of Abell 194, with the currently available exposures this question cannot be resolved.

We conclude that in regions A and B a $\gtrsim 2\sigma$ excess of point sources is detected, which may (partly) be due to unresolved features of the shocked X-ray gas and/or an excess population of bright sources.

6. MINKOWSKI'S OBJECT

Minkowski's Object (MO) (Minkowski 1958) lies along the jet emanating from NGC541 (PKS 0123-016A), and is a classic example of jet-triggered star-formation in the local Universe (Fig. 1). MO was studied by van Breugel et al. (1985) and Brodie et al. (1985), who suggested that the observed emission originated in a starburst. More recently a multi-wavelength study by Croft et al. (2006) found that the stellar population of MO is dominated by a 7.5×10^6 years old, 1.9×10^7 M$_\odot$ instantaneous burst, with a current SFR of 0.52 M$_\odot$/yr.

In actively star-forming galaxies the dominant fraction of the observed X-ray emission is a combination of the population of HMXBs and the diffuse hot ISM (e.g. Grimm et al. 2003; Bogdán & Gilfanov 2011). However, due to the relatively high source detection sensitivity $(\approx 7 \times 10^{38}$ erg s$^{-1})$ in MO, most of the HMXBs are not resolved. Indeed, in a circular region with $15''$ radius around MO we detected only one X-ray source with 8 net counts. Thus, in MO the various X-ray emitting components cannot be separated from each other since they all contribute to the unresolved emission. Therefore we can only place upper limits on the observed X-ray emission by assuming that it originates either from unresolved HMXBs or from hot ISM.

First, we assume that the total X-ray luminosity is due to the population of unresolved HMXBs. The observed source counts from the selected $15''$ circular region in the $0.5-8$ keV band correspond to a luminosity of $(2.3 \pm 0.4) \times 10^{39}$ erg s^{-1} assuming a typical HMXB power law spectrum with slope of $\Gamma = 2$ and Galactic column density. Converting this luminosity into the $2-10$ keV band, and taking into account the SFR in MO (Croft et al. 2006), we obtained L_X/SFR= $(2.7 \pm 0.4) \times 10^{39}$ (erg/s)/(M$_\odot$/yr). This value is in good agreement with that observed for HMXBs (Grimm et al. 2003; Shtykovskiy & Gilfanov 2005), thereby suggesting that, at least part of, the observed X-ray emission originates from the population of HMXBs.

Second, we assume that the observed X-ray emission is due to hot ISM. Since the observed number of counts is not enough to perform a spectral fit, we adopt a gas temperature of $kT = 1$ keV and 0.4 Solar abundance. Applying this conversion the observed counts correspond to a luminosity of $(1.0 \pm 0.2) \times 10^{39}$ erg s^{-1}. Assuming a spherically symmetric gas distribution within the selected $15''$ circular region, the estimated average gas density is 4.4×10^{-3} cm^{-3} and the total gas mass in MO is 7×10^7 M$_\odot$. Note that the upper limit on the gas mass is factor of ~ 4 times higher than the stellar mass in MO (Croft et al. 2006). Therefore it is unlikely that the hot ISM dominates the observed X-ray emission. Additionally, if the X-ray emission in MO is dominated by hot ISM, the associated thermal energy is on the order of few times 10^{56} erg, the exact value depending on the gas temperature. To inject this large amount of energy into the hot ISM, few times 10^5 Type Ia Supernova (SN Ia) explosions are required. On a timescale of 7.5×10^6 years, this implies a SN Ia rate of few times 10^{-2} yr^{-1}, being $1-2$ orders of magnitude higher than the predicted SN Ia rate in MO based on its SFR (Sullivan et al. 2006; Croft et al. 2006). Therefore SNe Ia cannot heat 7×10^7 M$_\odot$ gas to X-ray temperatures but only a small fraction of it. Thus, we conclude, that the X-ray emission in MO is either dominated by HMXBs or the jet interaction with the ambient ISM plays a role in heating

the gas.

7. CONCLUSIONS

We investigated the poor cluster, Abell 194, based on *Chandra* and *ROSAT* observations. The main results of our work are outlined below.

(i) We demonstrated the existence of an X-ray cavity at the southern part of Abell 194 formed by the southern radio lobe arising from 3C 40. Using the parameters of the hot ICM, the extent and location of the cavity, we estimated the total work of the AGN, 3.3×10^{59} erg, the age of the cavity, $t = 7.9 \times 10^7$ years, and the total cavity power, $P_{cav} = 1.3 \times 10^{44}$ erg s^{-1}.

(ii) We detected sharp surface brightness edges, identified as merger cold fronts, and extended tails in the *Chandra* images of NGC545 and NGC541. We estimated that NGC545 and NGC541 are moving with transonic velocities, and their motion is oriented approximately in the plane of the sky. Based on these and earlier observations, we concluded that NGC547, associated with 3C 40, lies at the center of Abell 194 and NGC545 and NGC541 are falling through the cluster.

(iii) A $\gtrsim 2\sigma$ excess of point sources were detected around the massive early-type galaxies in Abell 194. The additional sources may be (partly) due to unresolved features of the shocked X-ray gas in the coronae of the galaxies and/or an excess population of bright sources.

(iv) We also investigated the X-ray emission from Minkowski's Object, and concluded that it is most likely dominated by the population of HMXBs rather than by hot diffuse ISM.

REFERENCES

Allen, M. G., Sparks, W. B., Koekemoer, A., Martel, A. R., O'Dea, C. P., Baum, S. A., Chiaberge, M., Macchetto, F. D., Miley, G. K., 2002, ApJS, 139, 411

Andernach, H., Waldthausen, H. & Wielebinski, R., 1980, A&AS, 41, 339

Anders, E. & Grevesse, N., 1989, GeCoA, 53, 197

Baum, S. A., Heckman, T. M., Bridle, A., van Breugel, W. J. M. & Miley, G. K., 1988, ApJS, 68, 643

Birzan, L., Rafferty, D. A., McNamara, B. R., Wise, M. W. & Nulsen, P. E. J., 2004, ApJ, 607, 800

Birzan, L., McNamara, B. R., Nulsen, P. E. J., Carilli, C. L. & Wise, M. W., 2008, ApJ, 686, 859

Boehringer, H., Voges, W., Fabian, A. C., Edge, A. C. & Neumann, D. M., 1993, MNRAS, 264, L25

Bogdán, Á., Gilfanov, M., 2008, MNRAS, 388, 56

Bogdán, Á., Gilfanov, M., 2010, MNRAS, 405, 209

Bogdán, Á., Gilfanov, M., 2011, MNRAS, 412, 401

Brodie, J. P., Bowyer, S. & McCarthy, P., 1985, ApJ, 293, L59

Buttiglione, S., Capetti, A., Celotti, A., Axon, D. J., Chiaberge, M., Macchetto, F. D. & Sparks, W. B., 2009, A&A, 495, 1033

Buttiglione, S., Capetti, A., Celotti, A., Axon, D. J., Chiaberge, M., Macchetto, F. D. & Sparks, W. B., 2010, A&A, 509, 6

Chapman, G. N. F., Geller, M. J. & Huchra, J. P., 1988, AJ, 95, 999

Churazov, E., Brüggen, M., Kaiser, C. R., Böhringer, H. & Forman, W., 2001, ApJ, 554, 261

Croft, Steve, van Breugel, W., de Vries, W., Dopita, M., Martin, C., Morganti, R., Neff, S., Oosterloo, T., Schiminovich, D., Stanford, S. A. & van Gorkom, J., 2006, ApJ, 647, 1040

David, L. P., Nulsen, P. E. J., McNamara, B. R., Forman, W., Jones, C., Ponman, T., Robertson, B. & Wise, M., 2001, ApJ, 557, 546

Dickey, J. M., Lockman, F. J., 1990, ARA&A, 28, 215

Fabian, A. C., 1994, ARA&A, 32, 277

Forman, W., Nulsen, P., Heinz, S., Owen, F., Eilek, J., Vikhlinin, A., Markevitch, M., Kraft, R., Churazov, E. & Jones, C., 2005, ApJ, 635, 894

Gilfanov, M., 2004, MNRAS, 349, 146

Grimm, H.-J., Gilfanov, M. & Sunyaev, R., MNRAS, 339, 793

Hudaverdi, M., Kunieda, H., Tanaka, T., Haba, Y, Furuzawa, A., Tawara, Y. & Ercan, E. N., 2006, PASJ, 58, 931

Irwin, J. A., Athey, A. E.; Bregman, J. N., 2003, ApJ, 587, 356

Jarrett, T. H., Chester, T., Cutri, R., et al., 2003, AJ, 125, 525

Jones, C. & Forman, W., 1999, ApJ, 511, 65

Kaastra, J. S., Tamura, T., Peterson, J. R., Bleeker, J. A. M., Ferrigno, C., Kahn, S. M., Paerels, F. B. S., Piffaretti, R., Branduardi-Raymont, G. & Böhringer, H., 2004, A&A, 413, 415

Kuehr, H., Witzel, A., Pauliny-Toth, I. I. K. & Nauber, U., 1981, A&AS, 45, 367

Machacek, M., Dosaj, A., Forman, W., Jones, C., Markevitch, M., Vikhlinin, A., Warmflash, A. & Kraft, R., 2005, ApJ, 621, 663

Markevitch, M. & Vikhlinin, A., 2007, PhR, 443, 1

Minkowski, R., 1958, PASP, 70, 143

Moretti, A., Campana, S., Lazzati, D. & Tagliaferri, G., 2003, ApJ, 588, 696

Nikogossyan, E., Durret, F., Gerbal, D. & Magnard, F., 1999, A&A, 349, 97

Peterson, J. R., Kahn, S. M., Paerels, F. B. S., Kaastra, J. S., Tamura, T., Bleeker, J. A. M., Ferrigno, C. & Jernigan, J. G., 2003, ApJ, 90, 207

Peterson, J. R. & Fabian, A. C., 2006, PhR, 427, 1

Sakelliou, I., Hardcastle, M. J. & Jetha, N. N., 2008, MNRAS, 384, 87

Shtykovskiy, P. & Gilfanov, M., 2005, MNRAS, 362, 879

Spinrad, H., Marr, J., Aguilar, L. & Djorgovski, S., 1985, PASP, 97, 932

Sullivan, M., et al., 2006, ApJ, 648, 868

van Breugel, W., Filippenko, A. V.;,Heckman, T. & Miley, G., 1985, ApJ, 293, 83

van der Wolk, G., Barthel, P. D., Peletier, R. F. & Pel, J. W., 2010, A&A, 511, 64

Vikhlinin, A., Markevitch, M. & Murray, S. S., 2001, ApJ, 551, 160